Biomineralized N-Doped CNT/TiO_2 Core/Shell Nanowires for Visible Light Photocatalysis

Won Jun Lee,[†] Ju Min Lee,[†] Saji Thomas Kochuveedu,[‡] Tae Hee Han,[†] Hu Young Jeong,[†] Moonkyu Park,[†] Je Moon Yun,[†] Joon Kwon,[†] Kwangsoo No,[†] Dong Ha Kim,[‡,*] and Sang Ouk Kim[†,*]

[†]Department of Materials Science and Engineering, KAIST, Daejeon, 305-701, Republic of Korea and [‡]Department of Chemistry and Nano Science, Division of Molecular and Life Sciences, Ewha Womans University, Seoul 120-750, Republic of Korea

ABSTRACT We report an efficient and environmentally benign biomimetic mineralization of TiO_2 at the graphitic carbon surface, which successfully created an ideal TiO_2/carbon hybrid structure without any harsh surface treatment or interfacial adhesive layer. The N-doped sites at carbon nanotubes (CNTs) successfully nucleated the high-yield biomimetic deposition of a uniformly thick TiO_2 nanoshell in neutral pH aqueous media at ambient pressure and temperature and generated N-doped CNT (NCNT)/TiO_2 core/shell nanowires. Unlike previously known organic biomineralization templates, such as proteins or peptides, the electroconductive and high-temperature-stable NCNT backbone enabled high-temperature thermal treatment and corresponding crystal structure transformation of TiO_2 nanoshells into the anatase or rutile phase for optimized material properties. The direct contact of the NCNT surface and TiO_2 nanoshell without any adhesive interlayer introduced a new carbon energy level in the TiO_2 band gap and thereby effectively lowered the band gap energy. Consequently, the created core/shell nanowires showed a greatly enhanced visible light photocatalysis. Other interesting synergistic properties such as stimuli-responsive wettabilites were also demonstrated.

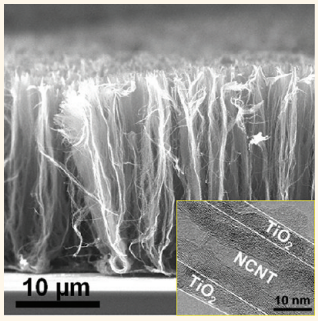

KEYWORDS: biomineralization · carbon nanotubes · doping · TiO_2 · photocatalysis

TiO_2 is a wide band gap semiconductor extensively used in pigments, sensors, electrodes, photocatalysts, and so on.[1−4] In particular, the photoexcitation of electron−hole pairs in TiO_2 may effectively sensitize or catalyze a light-induced redox process.[5,6] Nevertheless, the currently available TiO_2 photocatalysts generally suffer from a low surface area and a large band gap energy (3.2 eV), which significantly deteriorate the photocatalytic efficiency and effective range of a wavelength spectrum.[7,8] As an alternative, a hybrid of TiO_2 and graphitic carbon has gained tremendous research interest.[9−14] Ideal TiO_2/graphitic carbon hybrids reinforced with electroconductive and mechanically strong carbon nanotubes (CNTs) or a graphene backbone may possess an extremely large TiO_2/carbon interface that can facilitate electron−hole separation. Moreover, such interfacial hot spots may introduce a new carbon energy level in the TiO_2 band gap and thereby effectively lower the band gap energy.[15,16] Despite these conceptual advantages, currently available TiO_2/carbon hybrid fabrication methods require a high-temperature gas phase process,[17] harsh surface functionalization,[18] or an adhesive interlayer at the chemically inert graphitic carbon surface,[19,20] which can severely degrade the material properties of graphitic carbon materials as well as the effective charge transfer at the TiO_2/carbon interface.

Biomineralization is a natural synthetic route frequently employed by living organisms to create complex mineral architectures.[21−23] It generally attains a high-yield mineral deposition in a cost-effective, energy-efficient, and environmentally benign manner, which surpasses any other artificial methods of mineral deposition.[24−26] Moreover, the evolution of biomineral morphology can be precisely controlled over a broad range of length scales from nanometer to macroscopic scale to create a sophisticated hierarchical structure with remarkable three-dimensional conformality. Such enormous advantages have stimulated intensive research efforts to mimic biomineralization as an efficient method of mineral deposition.[27,28] Previous research has revealed that nitrogen (N)-containing organic molecules, including synthetic polymers as well as natural peptides, or proteins, can nucleate biomineralization.[29,30] Meanwhile, the low mechanical and thermal stability of those organic templates inherently limits the ultimate properties, including the thermal stability, of a biomineralized structure.[31,32]

* Address correspondence to dhkim@ewha.ac.kr, sangouk.kim@kaist.ac.kr.

Received for review November 19, 2011 and accepted December 23, 2011.

Published online December 23, 2011
10.1021/nn204504h

Because thermal calcination or other high-temperature processes are frequently involved in the formation of a dense mineral structure with desired crystal morphology, the low thermal stability inherently bottlenecks the ultimate use of biomineralization for functional material fabrication.

Here we present a straightforward fabrication of highly functional CNT/TiO_2 core/shell nanowires *via* biomimetic TiO_2 mineralization, which can be readily nucleated from the N-doped sites at CNTs.[33−35] Highly aligned vertical N-doped CNTs (NCNTs) were grown by plasma-enhanced chemical vapor deposition (PECVD) in an N environment.[36−39] The substitutional doping of electron-rich N effectively and permanently elevated the electrical conductivity as well as the surface wettability of CNTs.[40,41] Furthermore, N-doped sites successfully nucleated the biomimetic mineralization of a uniform nanoscale thick TiO_2 shell at the surface of NCNTs without any surface modification or adhesive interlayer. Taking advantage of the thermal stability of the NCNT backbone,[42,43] high-temperature annealing above 1000 °C could be conducted to transform the crystal structures of a low-crystalline as-mineralized TiO_2 layer into an anatase or a rutile phase without any damage to the nanowire morphology. Such idealized nanohybrids synergistically combining versatile TiO_2 and a graphitic carbon backbone without any interface modification demonstrated numerous interesting properties, including greatly enhanced visible light photocatalysis and stimuli-responsive wettability.

RESULTS AND DISCUSSION

Our biomimetic route to core/shell nanowires is schematically illustrated in Figure 1a. The mineralization was performed by a simple immersion of vertical NCNTs in a pH-controlled TiO_2 mineralization precursor solution for 2 h. The N-doped sites at the graphitic side walls of CNTs were exploited as the nucleation sites of the TiO_2 mineralization. Our PECVD growth generated two types of N-doping at the CNT surface: pyridinic N (N_P) and quaternary N (N_Q). Both types are believed to nucleate mineralization. For a uniform coverage of the TiO_2 nanoshell, a dense and uniform distribution of the nucleating sites as well as efficient nucleation mechanism was crucial. The distribution of N element along the CNTs could be confirmed by electron energy-loss spectroscopy (EELS). The atomic scale element mapping was supported by aberration-corrected high-resolution transmission electron microscopy (HR-TEM) imaging (Figure 1b−d; Supporting Information, Figure S1). Owing to the dense, evenly distributed N-doping sites, the biomimetic mineralization yielded highly uniform coverage of a ~5 nm thick TiO_2 nanoshell over the entire length of the vertical CNTs (Figure 1e,f; Supporting Information, Figure S2). The uniform encapsulation of the semiconducting TiO_2 nanoshell

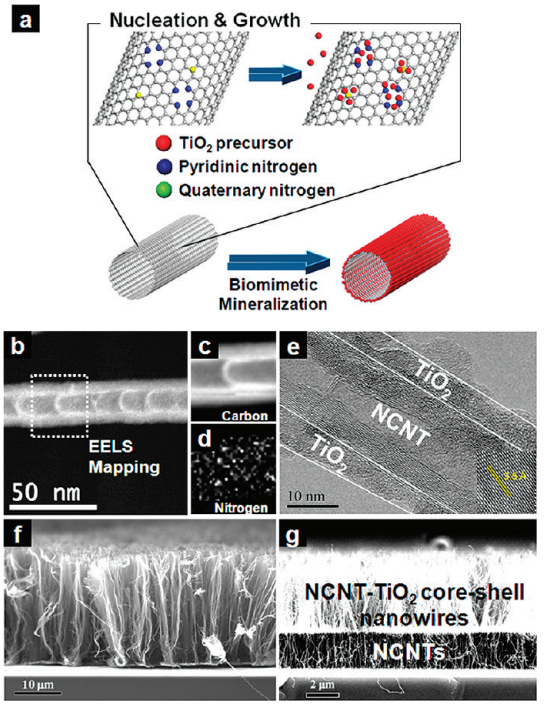

Figure 1. (a) Schematic illustration of biomimetic NCNT/TiO_2 core/shell nanowire fabrication. Red, blue, and yellow colors indicate TiO_2 precursor, pyridinic N (N_P), and quaternary N (N_Q), respectively. N-doping sites act as nucleation sites. (b) ADF-STEM image of NCNT. EELS mapping shows (c) C and (d) N elements along NCNT. (e) TEM and (f) SEM images of NCNT/TiO_2 core/shell nanowires. The inset shows the lattice distance of the anatase phase. (g) NCNT/TiO_2 core/shell (top) and bare NCNT(bottom) heteronanowires.

around a metallic NCNT was confirmed by the electrical conductivity measurements employing conductive atomic force microscopy (C-AFM; Supporting Information, Figure S3). While the NCNT showed a typical ohmic behavior, the core/shell nanowires exhibited the semiconducting behavior of a TiO_2 nanoshell.

After the biomimetic mineralization, the slow evaporation of the aqueous residue caused the collapse and aggregation of the core/shell nanowires. To maintain the individually separated vertical morphology,[44] we performed rapid vacuum drying at an ambient temperature. The rapid evaporation of the aqueous reside and subsequent calcinations at 500 °C generated highly aligned NCNT/anatase TiO_2 core/shell nanowires with a height of ~30 μm (Figure 1e inset and Figure 1f). Interestingly, the vertical NCNT growth had the potential to continue even after the TiO_2 mineralization. Our PECVD growth conditions provided a bottom growth, with the remaining Fe catalyst as the bottom substrate. When the NCNT growth conditions (C_2H_2 (5 sccm), NH_3 (40 sccm), and H_2 (60 sccm) at 750 °C) were imposed after the TiO_2 mineralization, the subsequent bottom growth of the NCNTs from the remaining catalysts created heterostructured nanowires where only the top parts were encapsulated by the TiO_2 shell (Figure 1e; Supporting Information, Figure S2e). We note

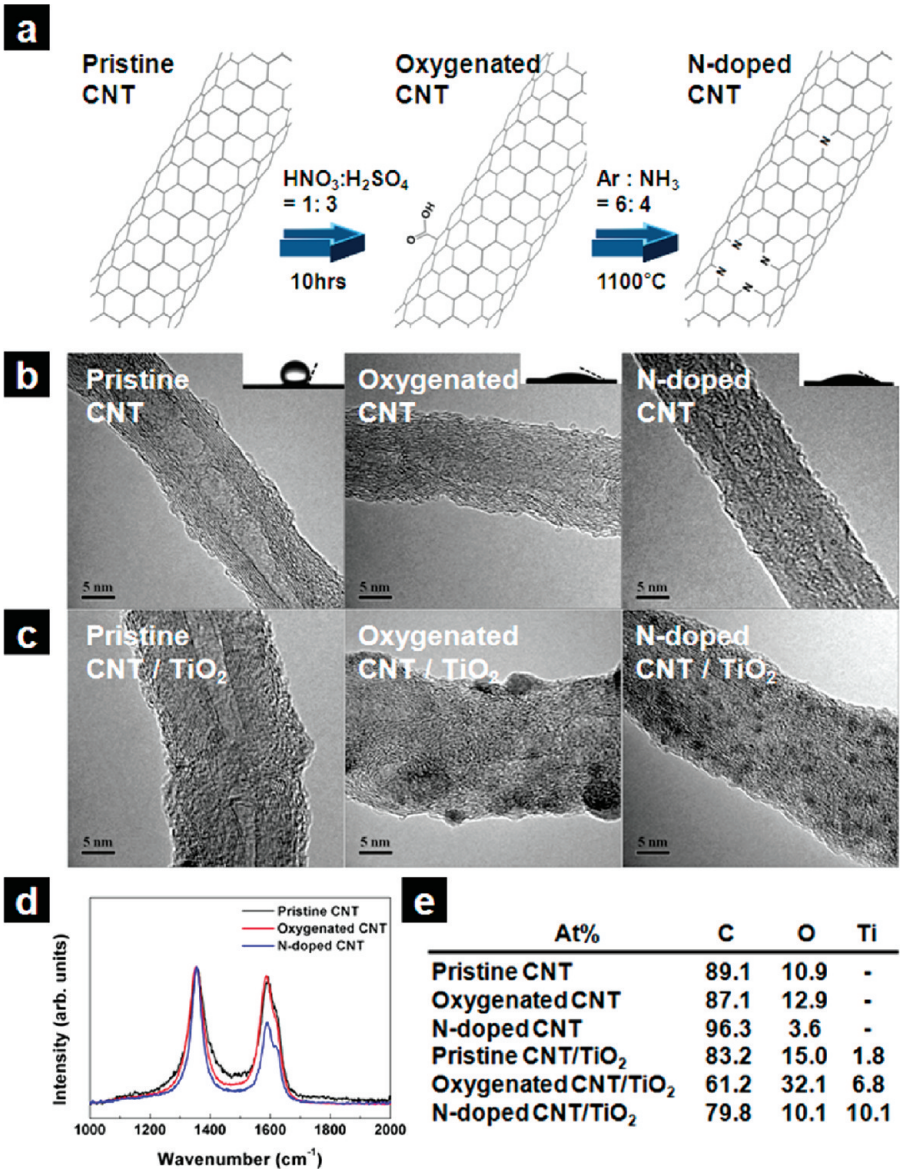

Figure 2. (a) Biomimetic TiO_2 mineralization of pristine, oxygenated, and N-doped CNTs. We note that all samples were prepared from commercial multiwalled CNTs for this control experiment. TEM images and water contact angles of (b) pristine CNTs (left), oxygenated CNTs (middle), and N-doped CNTs (right). TEM images of biomimetically TiO_2 mineralized (c) pristine CNTs (left), oxygenated CNTs (middle), and N-doped CNTs (right). (d) FT-Raman spectra of pristine, oxygenated, and N-doped CNTs. (e) Elemental analyses (atom %) calculated by EDX.

that the sharp and flat bottom ends of the TiO_2 shell signify that the previous biomimetic mineralization had been completed down to the bottom ends of the vertical NCNTs.

The efficient nucleating role of N-doped sites was investigated by the control experiments with undoped CNTs, acid-treated oxygenated CNTs, and N-doped CNTs, as presented in Figure 2. We note that all samples for these control experiments were prepared from commercially available multiwalled CNTs by post-thermal treatments. The detailed preparation procedures for oxygenated CNTs and N-doped CNTs are provided in the Experimental Section. While pristine, undoped CNTs have low-energy surfaces generally inappropriate for surface functionalization, oxygenated CNTs have high-energy surfaces with reactive oxygen-containing surface functionalities such as carboxylic acids and hydroxyl groups. Nonetheless, the same biomimetic mineralization conditions yielded a barely or only a partially mineralized morphology, as revealed by HR-TEM and energy dispersive X-ray spectroscopy (EDX) (Figure 2a,b). The distinct contrast in mineralized morphologies with N-doped CNTs (Figure 2c) provides strong evidence that N-doped sites play a nucleating role in biomimetic mineralization.

Unlike other thin film deposition methods that usually require a high-temperature or chemically harsh conditions, biomineralization is known to occur in environmentally benign mild conditions with a neutral pH and ambient pressure and temperature, where living

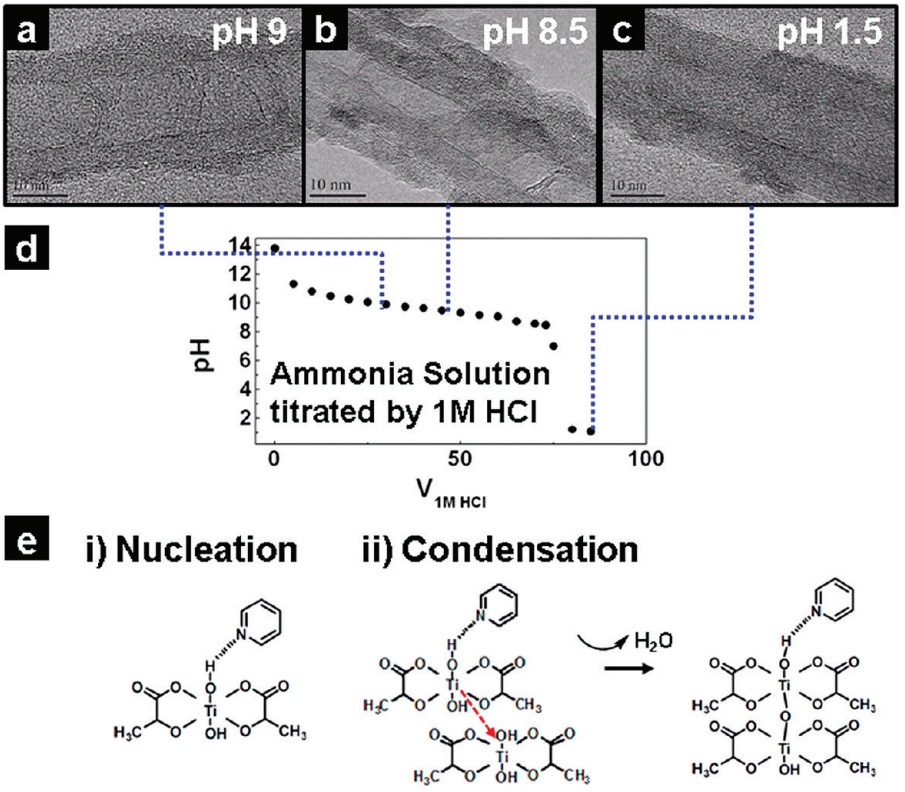

Figure 3. TEM images of biomimetic TiO_2 mineralization of NCNTs at various pH values of (a) 9, (b) 8.5, and (c) 1.5, respectively. (d) pH variation during the titration of buffer solution prepared from 28% ammonia solution with 1 M HCl. (e) Proposed mechanism for biomimetic TiO_2 mineralization on NCNTs.

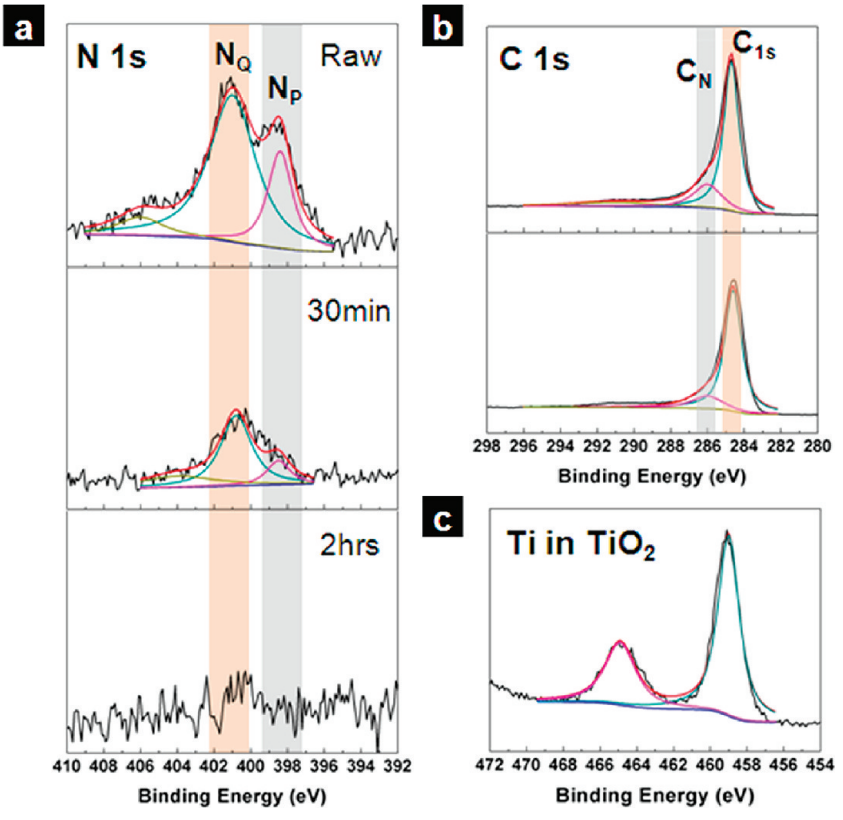

Figure 4. XPS spectra of NCNTs before and after biomimetic TiO_2 mineralization. (a) Variation of N peaks for N_P and N_Q before mineralization (top) and after 30 min (middle) and 2 h (bottom) of reaction, respectively. (b) C peaks for C_N and C_{1S} before mineralization (top) and after 2 h of reaction (bottom), respectively. (c) Ti peak for Ti_{2P} after 2 h of reaction.

organisms can survive. The influence of the pH upon the biomimetic mineralization of CNTs was exploited under conditions of ambient pressure and temperature, as shown in Figure 3. We prepared a mineralization solution from the 1:1 (v/v) mixtures of an aqueous buffered solution (NH_3 solution was titrated with 1 M of HCl) with a controlled pH (from 1.5 to 14) and a solution containing 50 wt % of titanium(IV) bis(ammonium lactato)dihydroxide. The HR-TEM images in Figure 3a–d show that the TiO_2 mineralization was successful only at a pH level of 8.5, which is consistent with a weak base condition for natural biomineralization.[45] In contrast, the samples mineralized at a slightly higher or lower pH level revealed a barely mineralized morphology.

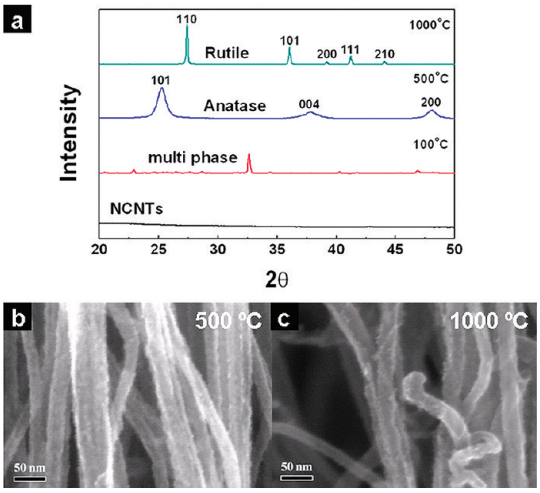

Figure 5. (a) XRD patterns of NCNT/TiO_2 core/shell nanowires annealed at 100, 500, and 1000 °C. SEM images of NCNT/TiO_2 core/shell nanowires after (b) 500 °C calcination and subsequent (c) 1000 °C calcination.

The surface chemistry of the NCNTs before and after TiO_2 mineralization was investigated by means of X-ray photoelectron spectroscopy (XPS; Figure 4). The N_{1s} peak of the raw NCNTs was deconvoluted into the peaks of N_P (398 eV) and N_Q (400.8 eV). The N_P peak became remarkably weakened during the first 30 min of mineralization. After 2 h, the entire N_{1s} peak became undetectable. Similar behavior was observed for the C_N peak, while the C_{1s} peak preserved its high intensity. This selective weakening of the N-involved peaks provides further evidence for the nucleating role of N-doped sites. Based on the obvious nucleating role of N-doped sites, a reaction mechanism is suggested for the biomimetic TiO_2 mineralization at NCNT surfaces.[46,47] As shown in Figure 3e, the TiO_2 mineralization occurs *via* the two stages of (i) nucleation and (ii) condensation. In the nucleation stage, the doped N is protonated and subsequently attracts and concentrates negatively charged TiO_2 precursors *via* electrostatic interaction and

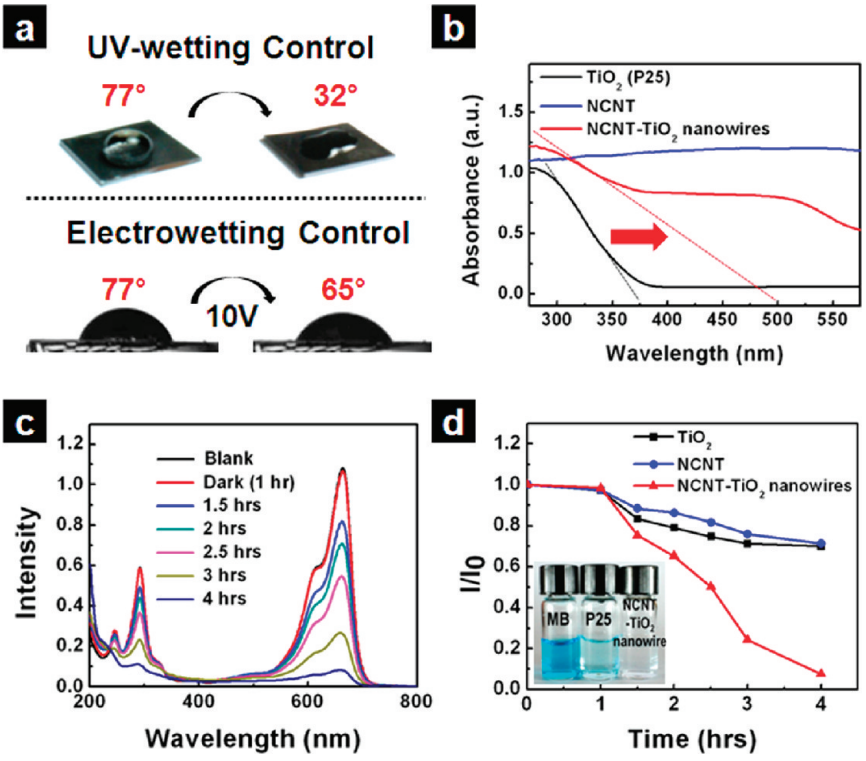

Figure 6. (a) Stimuli-responsive wetting behaviors of vertical NCNT/TiO_2 core/shell nanowire forests by UV radiation (top) and electrical potential (bottom). (b) UV–vis diffuse reflectance absorption spectra of the TiO_2, NCNT, and NCNT/TiO_2 core/shell nanowires. (c) Variation of absorption spectra of MB solution under visible light (λ = 420 nm) irradiation in the presence of NCNT/TiO_2 nanowires. (d) Visible light-induced MB degradation in the presence of TiO_2 (black) and NCNT/TiO_2 nanowires (red). Inset photograph compares the color of MB solution (10 ppm) after 3 h of visible light irradiation in the presence of NCNT/TiO_2 nanowires and P-25 commercial TiO_2 photocatalyst.

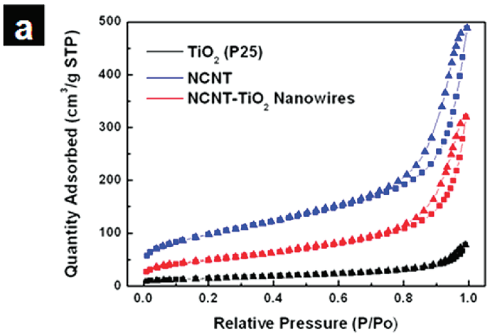

c

	BET Surface Area (m^2/g)	Pore Volume (cm^3/g)	Pore Size (nm)
P25	51.44	0.12	9.33
NCNT	351.97	0.76	8.58
NCNT-TiO_2 nanowires	177.50	0.49	11.15

Figure 7. (a) N_2 adsorption–desorption isotherm (squares, adsorption; triangles, desorption) and (b) Branauer–Emmet–Teller surface area plot of NCNT/TiO_2 nanowires. (c) Table showing the surface area, pore volume, and pore size of pure TiO_2 (P-25), NCNT, and NCNT/TiO_2 nanowires, respectively.

hydrogen bonding. After sufficient concentration of the precursors, nucleophilic substitution of Ti–O and a subsequent condensation occur. In this regard, the N-doped sites play two major roles, as adsorption sites and nucleating centers. Meanwhile, as shown in the X-ray diffraction (XRD) pattern of Figure 5a, the as-mineralized TiO_2 shell had poor crystallinity. The thermally stable CNT backbone allows high-temperature annealing, even above 1000 °C, which is generally prohibited for biominerals nucleated from organic templates such as peptides and proteins. While the thermal annealing at 500 °C formed a black anatase phase, the subsequent annealing at 1000 °C induced a more stable brown rutile phase, securing the core/shell nanowire morphology (Figure 5).

Dense and vertical NCNT/TiO_2 core/shell nanowires demonstrated versatile functionalities that synergistically combined the semiconducting TiO_2 and the large surface area metallic NCNT backbone, as presented in Figure 6. At first, the surface energy of the vertical core/shell nanowires was tunable by external stimuli, such as ultraviolet (UV) irradiation or electric potential.[48,49] The variation of surface energy could be visualized with measurements of the water contact angle. The initial contact angle at the surface of the vertical core/shell nanowire forest was 77° ± 1°. After the UV irradiation, the contact angle was significantly reduced to 32° ± 1° as a result of the reconstruction of the surface hydroxyl groups at the TiO_2 shell (Figure 6a, top image). The reconstruction of the surface hydroxyl groups is known to be driven by photoexcited electron–hole pairs. Reinforcement of the electroconductive NCNT core also enables the surface energy to be modified by electric potential, which had been hardly observed in the less electroconductive pure TiO_2-based materials (Supporting Information, Figure S4). As shown in Figure 6a, a potential of 10 V diminished the contact angle by 12°.

Our core/shell nanowires also demonstrated photocatalysis, whose efficiency was greatly enhanced by the nanoscale hybrid structure. As mentioned above, a direct interface of TiO_2 and CNTs without an adhesive interlayer can generate a new energy level in the middle of the TiO_2 band gap and thereby facilitate the electron transfer to CNTs under the photoexcitation.[50–52] The residual hole may then react with, and decompose, the chemicals that are adsorbed at the TiO_2 surface. The UV–vis diffuse reflection spectra (DRS) shown in Figure 6b confirm the generation of a new energy level. Compared with the pure TiO_2, there was an obvious red shift of ~120 nm in the absorption edge of the NCNT/TiO_2 nanowires. The generation of a carbon band caused the narrowing of the band gap and the corresponding red shift.[53] The enhanced photocatalysis under visible light irradiation (λ = 420 nm) was characterized by the photocatalytic degradation of a 10 ppm methylene blue (MB) and *p*-nitrophenol (PNP) solution in the presence of commercial TiO_2 (P-25) and NCNT/TiO_2 core/shell nanowires (Supporting Information, Figures S5–S7).[54] As evident in the color contrast after 3 h (Figure 6d inset), the photocatalysis of the NCNT/TiO_2 core/shell nanowires surpassed that of the widely used commercial TiO_2 catalyst. The decay of the UV absorbance intensity showed that the MB was almost completely degraded after 4 h in the presence of the core/shell nanowires, whereas ~70% of the MB remained in the presence of the P-25 commercial catalyst (Figure 6c and d). The remarkably enhanced photocatalysis was attributed to not only the band gap narrowing but also the large surface area of the core/shell nanowires in the aspects of charge transportation and adsorption. Figure 7 summarizes the Branauer–Emmet–Teller surface area, pore volume, and pore size of P-25, the NCNTs, and the NCNT/TiO_2 core/shell nanowires. The core/shell nanowires obviously had more than three times the surface area of pure TiO_2.

CONCLUSION

A process that mimics natural biomineralization could be used to readily synthesize versatile core/shell nanowires consisting of TiO_2 nanoshells uniformly wrapped around NCNT cores, without any adhesive interlayer. N-doped sites on the NCNT attracted Ti precursors and promoted their condensation to form

a highly uniform TiO_2 nanoshell with excellent coverage. Unlike other biomineralization nucleating templates such as protein or peptides, the electroconductive and thermally stable NCNT backbone enabled high-temperature treatment that optimized the corresponding crystal structure and properties of TiO_2 nanoshells. As representative examples of synergistic properties of core/shell nanowires, stimuli-responsive surface wetting and enhanced photocatalysis have been demonstrated. This idealized versatile TiO_2/graphitic carbon hybrid nanostructure inspired from an energy-efficient environmentally benign natural process would be useful for various artificial applications, including sensors, catalysts, and energy storage and conversion.

EXPERIMENTAL SECTION

Vertical NCNT Growth by PECVD. A 2 nm thick Fe catalyst film was deposited on a silicon substrate by means of e-beam evaporation. The substrate was heated to 750 °C in a gas flow mixture of H_2 and NH_3 (chamber pressure: 0.4 Torr). The NH_3 content was fixed at 40 vol % (H_2: 60 sccm, NH_3: 40 sccm). The thermal annealing (usually for less than 3 min) transformed the Fe film into agglomerated Fe nanoparticles. The chamber pressure was increased to 4.5 Torr, and dc plasma was activated with an anode dc voltage of 470 V relative to the grounded substrate. Slow streaming of an acetylene source gas at a flow rate of 5 sccm for 3 min produced dense vertical NCNTs from the catalyst particles.[40] At these conditions, we obtained 4.1 at. % nitrogen-doped CNT (carbon: 94 at. %, oxygen: 1.4%, iron: 0.5 at. % from XPS results).

Preparation of Oxygenated CNTs from Commercial Multiwalled CNTs. Multiwalled CNTs with a purity of 95% were purchased from Hanwha Nanotech. The 2 g of CNTs was sonicated in a 1:3 (125 mL/375 mL) mixture of HNO_3 (extra pure, Junsei) and H_2SO_4 (95−97%, Merck) for 10 h to generate oxygen functional groups; they were subsequently thermally treated at 400 °C for 40 min in air to remove any amorphous carbon species.[55,56]

Preparation of N-Doped CNTs from Commercial Multiwalled CNTs. For N-doping of commercial multiwalled CNTs, the oxygenated CNTs were thermally treated at 1100 °C for 4 h under a gas flow of Ar (40 sccm) and NH_3 (60 sccm).[57]

Biomimetic TiO_2 Mineralization of NCNTs. Prior to mineralization, all the CNTs (the vertical NCNTs, the pristine CNTs (as received), the oxygenated CNTs, and the N-doped CNTs) were dipped in ethanol for 1 min to enhance wettability. The TiO_2 mineralization was performed by placing the CNTs for 2 h in a 1:1 (v/v) mixture of aqueous buffered solution (3 mL of 28% ammonia solution (Junsei) titrated with 1 M HCl (Sigma-Aldrich)) with a pH range of 1.5 to 14 and a 3 mL of solution containing 50 wt % of titanium(IV) bis(ammonium lactato)dihydroxide (Aldrich). The pH of the aqueous buffered solution was changed by addition of 1 M HCl into the 28% ammonia solution. The excess physisorbed TiO_2 was rinsed away 10 times with water.

Calcination and Crystallization of NCNT/TiO_2 Core/Shell Nanowires. The TiO_2 mineralized NCNTs were annealed at 100 °C for 30 min in a high vacuum. To obtain a high crystalline anatase phase, we annealed the NCNT/TiO_2 nanowires at 500 °C for 2 h in air. A further 2 h of heat treatment was applied at 1000 °C in a high vacuum to obtain the rutile phase.

Characterization. The EELS mapping and spectra of the NCNTs were characterized with corrected scanning TEM (JEOL JEM-ARM200F, Japan). The morphologies of all the CNTs, before and after mineralization, were characterized with the aid of field-emission scanning electron microscopy (Hitachi S-4800 SEM, Japan) and HR-TEM (JEOL JEM-2100F). TEM EDX and multipurpose XPS (Thermo VG Scientific, Sigma Probe) were used for the chemical analysis of CNTs, before and after the TiO_2 mineralization. A Rigaku D/MAX-2500 diffractometer with Cu Kα irradiation (λ = 1.5418 Å) was used for the XRD measurements. The Raman spectra were recorded on a Bruker FT-Raman spectrometer (RFS 100/S) with an excitation wavelength of 1064 nm and a laser power of 20 mW. A topography image and the current response at a bias of applied voltage were investigated by using C-AFM (SPA 400, Seiko) with a Pt-coated AFM tip (EFM tips, Nanosensors). UV−vis DRS were recorded with a UV−vis spectrometer equipped with a SA-13.1 diffuse reflector (Scinco S-4100, Korea).[58]

Measurement of Water Contact Angle. Variations in the water contact angles of the vertical NCNT/TiO_2 core−shell nanowire forest, before and after UV irradiation or the application of electric potential, were measured with a contact angle analyzer in a static mode (Phoenix 150, SEO). The UV-responsive wetting variation was observed in samples exposed to UV light (wavelength: 254 nm; power: 25 W cm^{-2}; and XX-15S; UVP Inc.) for 10 min at room temperature. For the application of electric potential, samples were transferred to an ITO substrate by means of HF immersion. The subsequent change in surface wetting behavior was observed with a dc voltage of 10 V.

Photocatalysis Measurement. MB solution (10 ppm) and *p*-nitrophenol solution (10 ppm) were prepared in water, and 3.5 mL of the solution was transferred to quartz cuvettes. Samples (with dimensions of 0.8 cm × 0.8 cm) were placed in the cuvettes filled with the MB solution or *p*-nitrophenol solution. The samples were kept in the dark for 1 h to check the adsorption of dye on the surface of the catalyst. The cuvettes were then exposed to UV light (254 nm, 25 W cm^{-2}, and XX-15S; UVP Inc.) at room temperature. In the case of visible light photocatalysis, the cuvettes were irradiated by a Xe lamp (Newport Co. Ltd., model 66984) equipped with a 420 nm cutoff filter at a power of 450 W as a visible light source. The decrease in absorbance of one of the characteristic peaks of MB and *p*-nitrophenol was measured after various reaction times using UV−vis absorbance spectroscopy (Varian Cary5000 UV−vis−NIR spectrophotometer).

Acknowledgment. This work was supported by the National Research Laboratory Program (R0A-2008-000-20057-0), Converging Research Center Program (2011K000642), and the World Premier Materials (WPM) Program (10037689) funded by the Korean government. D.H.K. acknowledges a National Research Foundation of Korea (NRF) grant funded by the Korea government (MEST) (No. 20110002494).

Supporting Information Available: Supporting results. This material is available free of charge *via* the Internet at http://pubs.acs.org.

Note Added after ASAP Publication: This paper was published on the Web on December 29, 2011. The Acknowledgment section has been updated and the correct version reposted on January 24, 2012.

REFERENCES AND NOTES

1. Fujishima, A.; Rao, T. N.; Tryk, D. A. Titanium Dioxide Photocatalysis. *J. Photochem. Photobiol. C* **2000**, *1*, 1–21.
2. Baykin, D. V.; Friedrich, J. M.; Walsh, F. C. Protonated Titanates and TiO_2 Nanostructured Materials: Synthesis, Properties, and Applications. *Adv. Mater.* **2006**, *18*, 2807–2824.
3. Chen, X.; Mao, S. S. Titanium Dioxide Nanomaterials: Synthesis, Properties, Modifications, and Applications. *Chem. Rev.* **2007**, *107*, 2891–2959.
4. Han, T. H.; Oh, J. K.; Park, J. S.; Kwon, S.-H.; Kim, S.-W.; Kim, S. O. Highly Entangled Hollow TiO_2 Nanoribbons Templating Diphenylalanine. *J. Mater. Chem.* **2009**, *19*, 3512–3516.
5. Diebold, U. The Surface Science of Titanium Dioxide. *Surf. Sci. Rep.* **2003**, *48*, 53–229.
6. Thompson, T. L.; Yates., J. T., Jr. Surface Science Studies of the Photoactivation of TiO_2−New Photochemical Processes. *Chem. Rev.* **2006**, *106*, 4428–4453.

7. Zheng, Q.; Zhou, B.; Bai, J.; Li, L.; Jin, Z.; Zhang, J.; Li, J.; Liu, Y.; Cai, W.; Zhu, X. Self-Organized TiO_2 Nanotube Array Sensor for the Determination of Chemical Oxygen Demand. *Adv. Mater.* **2008**, *20*, 1044–1049.
8. Roy, P.; Berger, S.; Schmuki, P. TiO_2 Nanotubes: Synthesis and Applications. *Angew. Chem., Int. Ed.* **2011**, *50*, 2904–2939.
9. Banerjee, S.; Wong, S. S. Synthesis and Characterization of Carbon Nanotube-Nanocrystal Heterostructures. *Nano Lett.* **2002**, *2*, 195–200.
10. Kongkanand, A.; Dominguez, R. M.; Kamat, P. V. Single Wall Carbon Nanotube Scaffolds for Photoelectrochemical Solar Cells. Capture and Transport of Photogenerated Electrons. *Nano Lett.* **2007**, *7*, 676–680.
11. Yang, Y.; Qu, L.; Dai, L.; Kang, T.-S.; Durstock, M. Electrophoresis Coating of Titanium Dioxide on Aligned Carbon Nanotubes for Controlled Syntheses of Photoelectronic Nanomaterials. *Adv. Mater.* **2007**, *19*, 1239–1243.
12. Eder, D.; Windle, A. H. Carbon-Inorganic Hybrid Materials: The Carbon-Nanotube/TiO_2 Interface. *Adv. Mater.* **2008**, *20*, 1787–1793.
13. Leary, R.; Westwood, A. Carbonaceous Nanomaterials for the Enhancement of TiO_2 Photocatalysis. *Carbon* **2011**, *49*, 741–742.
14. Cong, Y.; Li, X.; Qin, Y.; Dong, Z.; Yuan, G.; Cui, Z.; Lai, X. Carbon-doped TiO_2 Coating on Multiwalled Carbon Nanotubes with Higher Visible Light Photocatalytic Activity. *Appl. Catal. B: Environ.* **2011**, *107*, 128–134.
15. Li, G.; Gray, K. A. The Solid-Solid Interface: Explaining the High and Unique Photocatalytic Reactivity of TiO_2-based Nanocomposite Materials. *Chem. Phys.* **2007**, *339*, 173–187.
16. Yao, Y.; Li, G.; Ciston, S.; Lueptow, R. M.; Gray, K. A. Photoreactive TiO_2/Carbon Nanotube Composites: Synthesis and Reactivity. *Environ. Sci. Technol.* **2008**, *42*, 4952–4957.
17. Joshi, R. K.; Engstler, J.; Navitski, A.; Sakharuk, V.; Müller, G.; Schneider, J. Gas Phase Synthesis and Field Emission Properties of 3D Aligned Double Walled Carbon Nanotube/Anatase Hybrid Architectures. *Nanoscale* **2011**, *3*, 3258–3264.
18. Li, Z.; Gao, B.; Chen, G. Z.; Mokaya, R.; Sotiropoulos, S.; Puma, G. L. Carbon Nanotube/Titanium Dioxide (CNT/TiO_2) Core-Shell Nanocomposites with Tailored Shell Thickness, CNT Content and Photocatalytic/Photoelectrocatalytic Properties. *Appl. Catal. B: Environ.* **2011**, *110*, 50–57.
19. Lee, S.-W.; Sigmund, W. M. Formation of Anatase TiO_2 Nanoparticles on Carbon Nanotubes. *Chem. Commun.* **2003**, 780–781.
20. Pender, M. J.; Sowards, L. A.; Hartgerink, J. D.; Stone, M. O.; Naik, R. R. Peptide-Mediated Formation of Single-Wall Carbon Nanotube Composites. *Nano Lett.* **2006**, *6*, 40–44.
21. Mann, S. Molecular Recognition in Biomineralization. *Nature* **1988**, *332*, 119–124.
22. Heuer, A. H.; Fink, D. J.; Laraia, V. J.; Arias, J. A.; Calvert, P. D.; Kendall, K.; Messing, G. L.; Blackwell, J.; Rieke, P. C.; Thompson, D. H.; *et al*. Innovative Materials Processing Strategies: A Biomimetic Approach. *Science* **1992**, *255*, 1098–1105.
23. Sanchez, C.; Arribart, H.; Madeleine, M.; Guille, G. Biomimetism and Bioinspiration as Tools for the Design of Innovative Materials and Systems. *Nat. Mater.* **2005**, *4*, 277–288.
24. Weiner, S.; Addadi, L. At the Cutting Edge. *Science* **2002**, *298*, 375–376.
25. Cölfen, H.; Mann, S. Higher-Order Organization by Mesoscale Self-Assembly and Transformation of Hybrid Nanostructures. *Angew. Chem., Int. Ed.* **2003**, *42*, 2350–2365.
26. Kröger, N.; Sandhage, K. H. From Diatom Biomolecules to Bioinspired Syntheses of Silica- and Titania-based Materials. *MRS Bull.* **2010**, *35*, 122–126.
27. Aksay, I. A.; Tray, M.; Manne, S.; Honma, I.; Yao, N.; Zhou, L.; Fenter, P.; Eisenberger, P. M.; Gruner, S. M. Biomimetic Pathways for Assembling Inorganic Thin Films. *Science* **1996**, *273*, 892–898.
28. Zhai, H.; Jiang, W.; Tao, J.; Lin, S.; Chu, X.; Xu, X.; Tang, R. Self-Assembled Organic-Inorganic Hybrid Elastic Crystal. *Adv. Mater.* **2010**, *22*, 3729–3734.
29. Anderson, K. D.; Marczewski, K.; Singamaneni, S.; Slocik, J. M.; Jakubiak, R.; Naik, R. R.; Bunning, T. J.; Tsukruk, V. V. Plasma Amino Acid Coatings for a Conformal Growth of Titania Nanoparticles. *ACS Appl. Mater. Interfaces* **2010**, *2*, 2269–2276.
30. Berrigan, J. D.; Kang, T.-S.; Cai, Y.; Deneault, J. R.; Durstock, M. F.; Sandhage, K. H. Protein-Enabled Layer-by-Layer Syntheses of Aligned Porous-Wall, High-Aspect-Ratio TiO_2 Nanotube Arrays. *Adv. Funct. Mater.* **2011**, *21*, 1693–1700.
31. Rodríguez-Hernández, J.; Babin, J.; Zappone, B.; Lecommadoux, S. Preparation of Shell Cross-Linked Nano-Objects from Hybrid-Peptide Block Copolymers. *Biomacromolecules* **2005**, *6*, 2213–2220.
32. Johnson, J. R., III; Spikowski, J.; Schiraldi, D. A. Mineralization of Clay/Polymer Aerogels: A Bioinspired Approach to Composite Reinforcement. *ACS Appl. Mater. Interfaces* **2009**, *1*, 1305–1309.
33. Zhi, L.; Hu, Y.-S.; Hamaoui, B. E.; Wang, X.; Lieberwirth, I.; Kolb, U.; Maier, J.; Müllen, K. Precursor-Controlled Formation of Novel Carbon/Metal and Carbon/Metal Oxide Nanocomposites. *Adv. Mater.* **2008**, *20*, 1727–1731.
34. Lee, S. H.; Kim, H. W.; Hwang, J. O.; Lee, W. J.; Kwon, J.; Bielawski, C. W.; Ruoff, R. S.; Kim, S. O. Three-Dimensional Self-Assembly of Graphene Oxide Platelets into Mechanically Flexible Macroporous Carbon Films. *Angew. Chem., Int. Ed.* **2010**, *49*, 10084–10088.
35. Lee, W. J.; Lee, D. H.; Han, T. H.; Lee, S. H.; Moon, H. -S.; Lee, J. A.; Kim, S. O. Biomimetic Mineralization of Vertical N-doped Carbon Nanotubes. *Chem. Commun.* **2011**, *47*, 535–537.
36. Lee, D. H.; Shin, D. O.; Lee, W. J.; Kim, S. O. Hierarchically Organized Carbon Nanotube Arrays from Self-Assembled Block Copolymer Nanotemplates. *Adv. Mater.* **2008**, *20*, 2480–2485.
37. Lee, D. H.; Kim, J. E.; Han, T. H.; Hwang, J. W.; Jeon, S. W.; Choi, S.-Y.; Hong, S. H.; Lee, W. J.; Ruoff, R. S.; Kim, S. O. Versatile Carbon Hybrid Films Composed of Vertical Carbon Nanotubes Grown on Mechanically Compliant Graphene Films. *Adv. Mater.* **2010**, *22*, 1247–1252.
38. Lee, S. H.; Lee, D. H.; Lee, W. J.; Kim, S. O. Tailored Assembly of Carbon Nanotubes and Graphene. *Adv. Funct. Mater.* **2011**, *21*, 1338–1354.
39. Lee, K. S.; Lee, W. J.; Kim, S. O.; Park, J. H. Transferred Vertically Aligned N-doped Carbon Nanotube Arrays: Use in Dye-Sensitized Solar Cells as Counter Electrodes. *Chem. Commun.* **2011**, *47*, 4264–4266.
40. Lee, D. H.; Lee, W. J.; Kim, S. O. Highly Efficient Vertical Growth of Wall-Number-Selected, N-Doped Carbon Nanotube Arrays. *Nano Lett.* **2009**, *9*, 1427–1432.
41. Lee, D. H.; Lee, W. J.; Lee, W. J.; Kim, S. O.; Kim, Y. −H. Theory, Synthesis, and Oxygen Reduction Catalysis of Fe-Porphyrin-Like Carbon Nanotube. *Phys. Rev. Lett.* **2011**, *106*, 175502.
42. Ruoff, R. S.; Lorents, D. C. Mechanical and Thermal Properties of Carbon Nanotubes. *Carbon* **1995**, *33*, 925–930.
43. Thostenson, E. T.; Ren, Z.; Chou, T.-W. Advances in the Science and Technology of Carbon Nanotubes and Their Composites: A Review. *Compos. Sci. Technol.* **2001**, *61*, 1899–1912.
44. Liu, H.; Li, S.; Zhai, J.; Li, H.; Zheng, Q.; Jiang, L.; Zhu, D. Self-Assembly of Large-Scale Micropatterns on Aligned Carbon Nanotube Films. *Angew. Chem., Int. Ed.* **2004**, *43*, 1146–1149.
45. Jin, R.-H.; Yuan, J.-J. Biomimetically Controlled Formation of Nanotextured Silica/Titania Films on Arbitrary Substrate and Their Tunable Surface Function. *Adv. Mater.* **2009**, *21*, 3750–3753.
46. Möckel, H.; Giersig, M.; Willig, F. Formation of Uniform Size Anatase Nanocrystals from Bis(ammonium lactato)titanium Dihydroxide by Thermohydrolysis. *J. Mater. Chem.* **1999**, *9*, 3051–3056.
47. Jiang, Y.; Yang, D.; Zhang, L.; Li, L.; Sun, Q.; Zhang, Y.; Li, J.; Jiang, Z. Biomimetic Synthesis of Titania Nanoparticles Induced by Protamine. *Dalton Trans.* **2008**, 4165–4171.
48. Kakade, B.; Mehta, R.; Durge, A.; Kulkarni, S.; Pillai, V. Electric Field Induced, Superhydrophobic to Superhydrophillic Switching in Multiwalled Carbon Nanotube Papers. *Nano Lett.* **2008**, *8*, 2693–2696.

49. Zhang, M.; Zhang, T.; Cui, T. Wettability Conversion from Superoleophobic to Superhydrophilic on Titania/Single-walled Carbon Nanotube Composite Coatings. *Langmuir* **2011**, *27*, 9295–9301.
50. Woan, K.; Pyrgiotakis, G.; Sigmund, W. Photocatalytic Carbon-Nanotube-TiO_2 Composites. *Adv. Mater.* **2009**, *21*, 2233–2239.
51. Xu, Y.-J.; Zhuang, Y.; Fu, X. New Insight for Enhanced Photocatalytic Activity of TiO_2 by Doping Carbon Nanotubes: A Case Study on Degradation of Benzene and Methyl Orange. *J. Phys. Chem. C* **2010**, *114*, 2669–2676.
52. Chen, W.; Fan, Z.; Zhang, B.; Ma, G.; Takanabe, K.; Zhang, X.; Lai, Z. Enhanced Visible-Light Activity of Titania *via* Confinement inside Carbon Nanotubes. *J. Am. Chem. Soc.* **2011**, *133*, 14896–14899.
53. Zhang, Y.; Tang, Z.-R.; Fu, X.; Xu, Y.-J. TiO_2-Graphene Nanocomposites for Gas-Phase Photocatalytic Degradation of Volatile Aromatic Pollutant: Is TiO_2-Graphene Truly Different from Other TiO_2-Carbon Composite Materias? *ACS Nano* **2010**, *4*, 7303–7314.
54. Kochuveedu, S. T.; Jang, Y. J.; Jang, Y. H.; Lee, W. J.; Cha, M. A.; Shin, H. Y.; Yoon, S. H.; Lee, S. S.; Kim, S. O.; Shin, K. W.; *et al*. Visible-Light Active Nanohybrid TiO_2/Carbon Photocatalysts with Programmed Morphology by Direct Carbonization of Block Copolymer Templates. *Green Chem.* **2011**, *13*, 3397–3405.
55. Lee, S. H.; Park, J. S.; Lim, B. K.; Mo, C. B.; Lee, W. J.; Lee., J. M.; Hong, S. H.; Kim, S. O. Highly Entangled Carbon Nanotube Scaffolds by Self-Organized Aqueous Droplets. *Soft Matter* **2009**, *5*, 2343–2346.
56. Lee, J. M.; Park, J. S.; Lee, S. H.; Kim, H.; Yoo, S.; Kim, S. O. Selective Electron or Hole Transport Enhancement in Bulk-Heterojunction Oranic Solar Cells with N- or B-Doped Carbon Nanotubes. *Adv. Mater.* **2011**, *23*, 629–633.
57. Hwang, J. O.; Park, J. S.; Choi, D. S.; Kim, J. Y.; Lee, S. H.; Lee, K. E.; Kim, Y.-H.; Song, M. H.; Yoo, S.; Kim, S. O. Workfunction-Tunable, N-Doped Reduced Graphene Transparent Electrodes for High-Performance Polymer Light-Emitting Diodes. *ACS Nano* (online-pubslished) DOI: 10.1021/nn203176u.
58. Xie, Y.; Ali, G.; Yoo, S. H.; Cho, S. O. Sonication-assisted Synthesis of CdS Quantum-Dot-Sensitized TiO_2 Nanotube Arrays with Enhanced Photoelectrochemical and Photocatalytic Activity. *ACS Appl. Mater. Interfaces* **2010**, *2*, 2910–2914.